Land-surface-atmosphere coupling in observations and models

Alan K. Betts

Atmospheric Research
Pittsford, VT 05763
akbetts@aol.com

1. Introduction

This review is a synthesis of my understanding of the physical processes involved in the land-surface-atmosphere interaction, illustrated using figures adapted from my published work, covering the past 15 years (so they reflect both my idiosyncrasies and as well as many aspects of the ECMWF model). I believe synthesis is always valuable, because of the complexity of the earth system. In section 2, I will discuss the surface energy balance, and the role of the surface and cloud albedos in the shortwave and longwave fluxes, and comment on the radiative scaling of the diurnal temperature range and the night-time boundary layer. Section 3 will deal with the role of water in the surface energy partition, vector methods for understanding mixed layer evolution, the coupling between surface and boundary layer and the impact of clouds on the surface energy partition. Finally, section 4 will discuss evaporation-precipitation feedback, the coupling of column water vapor, clouds and precipitation to vertical motion and moisture convergence over land in the tropics and compare the relation of surface shortwave cloud forcing and precipitation forcing of the atmosphere in ERA-40 with observations.

My frame is that of *land-surface climate*; not the details of synoptic weather, but the systematic features of the diurnal and seasonal cycle, and also the way processes are coupled on the daily timescale. How these are represented in the model, what is observable in nature and what are the underlying fundamental interrelated physical processes. Where possible, I will contrast relationships that are observable with how well they are simulated in the ECMWF model. Our observational datasets are however always incomplete; and key parameters, like soil moisture and the surface fluxes, are not measured on the scale of the model grid.

Two previous reviews (Betts et al., 1996; Betts, 2004) provide some background on my frame of reference and implicit assumptions. The first discusses the interaction of processes at the land-surface-atmosphere interface from both a modeling and an observational perspective, influenced heavily by my involvement in two field programs. One was the First ISLSCP (International Satellite Land Surface Climatology Project) Field Experiment, FIFE (Sellers et al., 1992), which took place over a grassland prairie near Manhattan, Kansas. The second was the Boreal Ecosystem-Atmosphere Study, BOREAS, (Sellers et al., 1997), which took place across the boreal forest of central Saskatchewan and Manitoba. This project was succeeded by the Boreal Ecosystem Research and Monitoring Sites, BERMS. Betts et al. (1996) discusses both these field program data and the ECMWF modeling perspective on soil moisture-atmosphere interactions, which were apparent in the development of the 4-layer land-surface model that was implemented operationally in 1993 (Viterbo and Beljaars, 1995). The ERA-40 modeling system introduced the TESSEL land-surface scheme (Van den Hurk et al., 2000); and Betts (2004) picked up this theme of soil moisture interactions, and addressed the issue of "Understanding hydrometeorology using global models" by mapping the coupling between different processes and observables at the land surface, using daily mean data from ERA-40.

As new parameterizations are developed and introduced, it is critical to look at how they interact in establishing the diurnal cycle and the daily mean state at the land surface. Accuracy and minimal drift in the

land-surface climate and the surface fluxes impact forecast skill on all timescales from the diurnal to the seasonal. As I write (in Vermont) in early August after weeks of above normal precipitation, the ground is saturated, mist rises from the forests in the mornings, cloud cover is extensive, reducing daily maximum temperatures and the diurnal temperature range, and afternoons are dominated by heavy rain from cumulonimbus and organized mesoscale convection systems. Flooding has washed out many roads. From a land-surface feedback perspective, I could be in the Amazon in the rainy season! Evaporation-cloud-precipitation feedback, coupled to the larger scale dynamics, plays an important role in warm season forecasts.

2.   Surface Energy Balance

The surface energy balance (SEB) has a large impact on the surface equilibrium climate and the diurnal temperature range. We will simplify it as

$$R_{net} = SW_{net} + LW_{net} = H + \lambda E + G \tag{1}$$

where the surface net radiation, R_{net}, is the sum of net shortwave and longwave fluxes; and it is balanced by the upward sensible heat flux, H, and latent heat flux, λE, and the storage, G, in the ground and the vegetation canopy. Eq. (1) for the SEB is a highly coupled system, but for understanding it will be broken down into components

- the split between SW and LW processes

- the split between surface processes and atmospheric processes

- the partition between clear-sky and cloud processes in the atmosphere

- the partition of the surface R_{net} into H and λE, which is controlled largely by the availability of water for evaporation and by vegetation

2.1.   Aside on land-ocean difference

Of course land and ocean are very different (eg. Betts, 2003). Over the ocean (and large lakes), the diurnal temperature range is small, because the incoming solar energy is mixed downward into an ocean "mixed layer", which is usually tens of meters deep. One day of solar heating will warm a layer of water 50m deep less than 0.1K, because of its large thermal capacity. Only in light winds, when the downward mixing is small, does the diurnal range of sea surface temperature reach 1K. On time-scales much longer than the diurnal, evaporation of water primarily balances the surface net radiation budget. The sensible heat flux is small and largely balances the radiative cooling of the sub-cloud layer (Betts and Ridgway, 1989). Over land, only a small fraction (<20%) of the net radiation at the surface is conducted downward in the daytime, or stored for example by warming trees on the surface. As a result, the land-surface temperature rises rapidly after sunrise, until near-balance is achieved between the net radiation and the sensible and latent heat fluxes to the atmosphere. If the surface is a desert, then the daytime temperature rise (and night-time fall) is large, but if water is readily available for evaporation or transpiration, the daytime rise of temperature is greatly reduced, because most of net radiation goes into the latent heat of vaporization. Higher surface albedos over land, as well as cloud cover, also play an important role in reducing the surface net radiation.

2.2.   Surface SW_{net}

This can be written in terms of the clear-sky downwelling flux, SW_{down}(clear) as

$$SW_{net} = SW_{down} - SW_{up} = (1 - \alpha_{surf})(1 - \alpha_{cloud}) SW_{down} (clear) \tag{2}$$

where the surface albedo, α_{surf}, is the ratio SW_{up}/SW_{down} and an *effective cloud albedo* is defined (Betts and Viterbo, 2005; Betts, 2007) from the surface short-wave cloud forcing, SWCF, as

$$\alpha_{cloud} = -SWCF/SW_{down}(clear) \tag{3}$$

where

$$SWCF = SW_{down} - SW_{down}(clear) \tag{4}$$

This *effective cloud albedo* α_{cloud} is just a non-dimensional measure of the surface shortwave cloud forcing. These two albedos play equivalent roles in the surface SW budget: α_{surf} is a function of surface properties, and may vary seasonally with vegetation cover and both daily and seasonally with snow and ice cover; while α_{cloud} is a function of boundary layer and atmospheric cloud processes, with variability on a wide range of timescales.
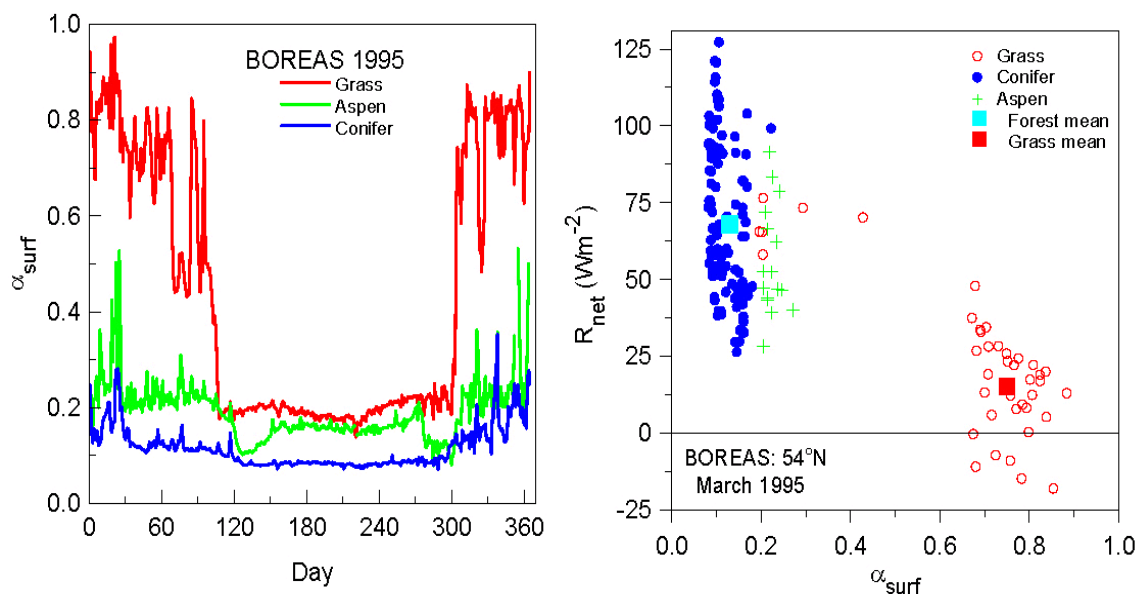

Figure 1: Surface albedo of conifer, aspen and grass (left); March R_{net} as a function of surface albedo (right)

2.3. Surface albedo

A background surface albedo is often specified in models (with a seasonal variation), while the contribution of snow is calculated. It is not however easy to determine either accurately from satellite data. Zhang et al. (2007) suggest that the uncertainty in surface broadband albedos derived from different global datasets is of order 7%. This is an area that needs more attention, because albedos errors generate large biases in the SEB, the surface temperature and the surface fluxes, which feed through to the troposphere. The impact of land cover, with and without snow, is large. Figure 1 (left panel) shows the surface albedo of conifer and aspen forests, and grass, composited from ten sites during the BOREAS experiment in Saskatchewan and Manitoba during calendar year 1995 (Betts and Ball, 1997). These are local measurements from towers over the forest, but they are from well-calibrated instruments. Measurements from satellites are better spatial means, but suffer from problems with radiometer calibration and cloud contamination. We see the characteristic differences in seasonal cycle. The conifer sites (spruce and pine) have the lowest albedo, below 0.1 in the summer and rarely above 0.2 in the winter, because the snow under the canopy is shaded from the sun at high zenith angles in winter. The deciduous aspen site has a higher albedo: note the spring and fall dips before leaf-out and after leaf-fall. The grass sites are close to 0.2 in summer and as high as 0.8 with snow

cover in winter. The climate implication of these differences are huge (eg Betts, R.A., 2000); as is the forecast impact, if the grid-point mean is misrepresented. Figure 1 (right panel) shows the scatter of daily mean measured R_{net} at these sites against α_{surf} for grass and forest sites for the month of March, and the means for grass and forest. The scatter is large vertically as the solar zenith angle is changing rapidly in March. The distinct clustering of the data is obvious. Except for a few points with no snow, the grass sites have far lower values of R_{net} than the forest sites. [A useful synthesis of the boreal ecosystem and its relation to climate is given in Hall et al. (2004).]

Changing the formulation of the surface albedo in the ECMWF model can have a radical impact on the lower troposphere over the northern continents, as shown in Figure 2. In the spring of 1996, the ECMWF model suffered from a large cold bias over the high latitude boreal forest regions. The main source of this error was that surface albedo with snow was of order 0.7-0.8, corresponding to grass rather than forest. In December 1996, the boreal forest albedo was limited to a maximum of 0.2 in the presence of snow (Viterbo and Betts, 1999). [The observations shown in Figure 1 indicate that this change will have a large impact on surface R_{net} in spring.] Figure 2 shows the remarkable reduction in the model systematic bias in 5-day 850 hPa temperature forecasts between March-April, 1996 and March-April, 1997, associated primarily with this reduction in surface albedo. In 1996, the temperature error grows to -6K over eastern Russia; while in 1997, these large errors are greatly reduced. The impact on forecast skill from this albedo change is large, and positive from February to May (Viterbo and Betts, 1999). This albedo change was made without revising other aspects of the land-surface scheme, which was then Viterbo and Beljaars (1995), with a globally fixed vegetative resistance to evaporation, also characteristic of grasslands rather than forests. As a result, the reduction of surface albedo in spring, which increased R_{net}, gave too much surface evaporation and precipitation. The introduction of a new land-surface model TESSEL (van den Hurk et al., 2000) came later. This reduced evaporation over the boreal forest by specifying a larger unstressed vegetative resistance for this vegetation class (Betts et al., 2001a).
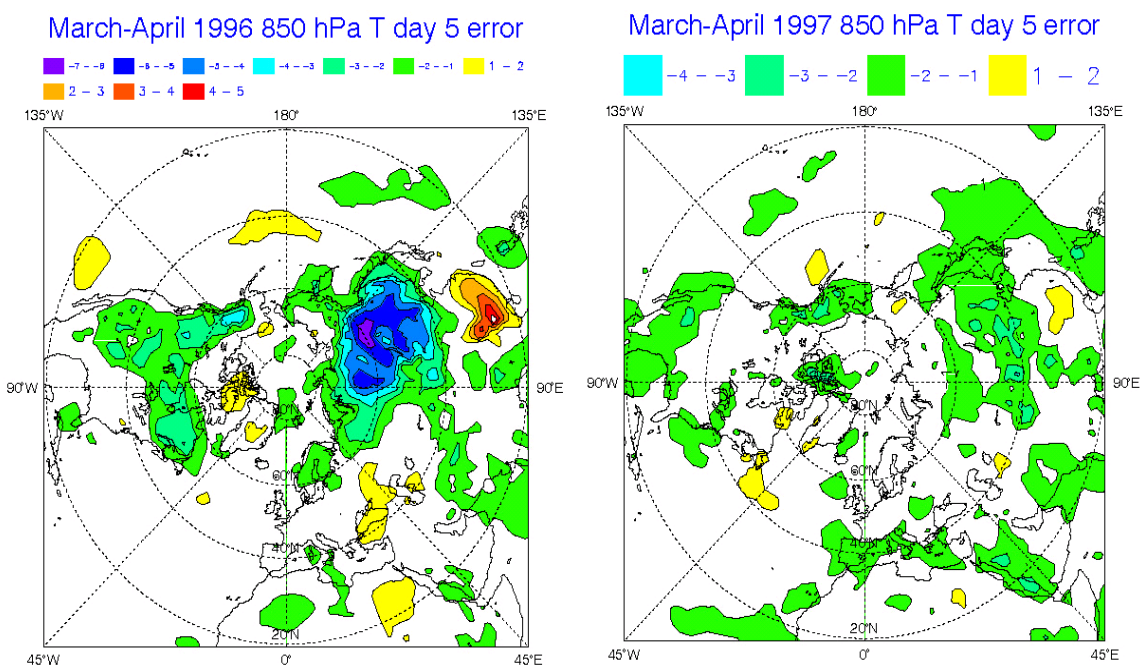

Figure 2: Mean 5-day 850 hPa forecasts temperature error for March-April, 1996 and March-April, 1997

2.4. Cloud albedo

The transformation from SWCF to effective cloud albedo is illustrated in Figure 3. The envelope of red points are the daily clear sky SW_{net} fluxes from ERA-40 for the Ohio-Tennessee river basin for the five years, 1996-2000 (Betts, 2007). The blue dots are the daily-mean all-sky SW_{net} fluxes. The transformation given by (3) and (4) gives us (using SW_{net} or SW_{down}) the right-hand panel of the daily mean α_{cloud}, scaled between 0 and 1. Note the wide scatter on the daily time-scale, associated with atmospheric processes that generate clouds: much more variability than in the surface albedo. But there is mean seasonal structure here. The solid curves show the monthly means for this period for ERA-40 (red) and the ISCCP data (green). Except in summer, ERA-40 has too little reflective cloud. The error bars are the interannual variability of the bias, ERA40-ISCCP, showing that, although cloud cover is a noisy variable on the daily timescale, the mean bias of ERA-40 is significant. From a climate and a SEB perspective, we see from (2) that a 10% error in α_{cloud} is just as significant as a 10% error in the surface albedo.
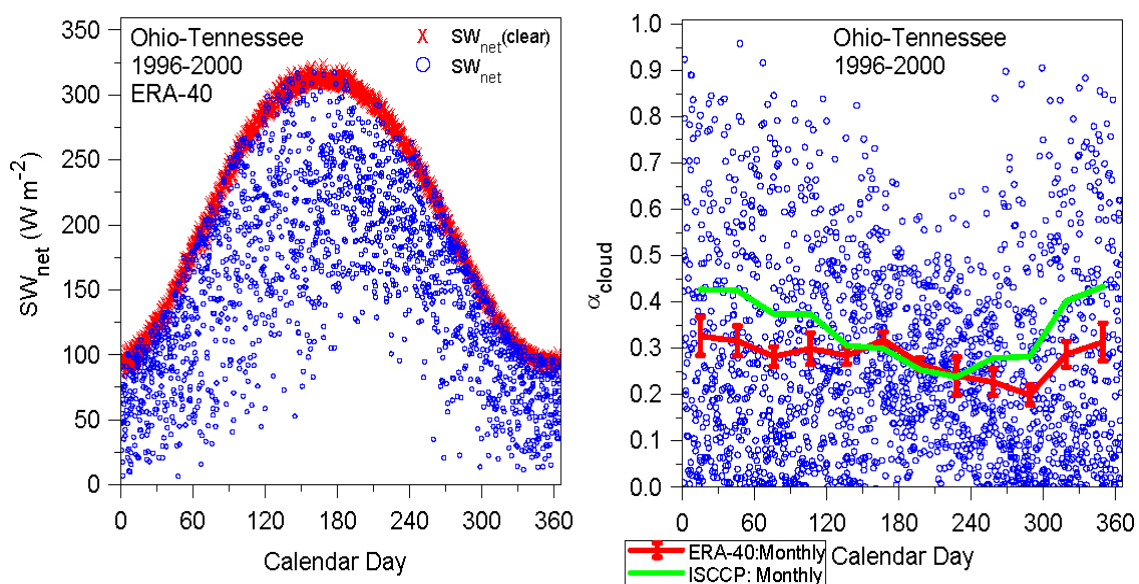

Figure 3: Daily-mean SW_{net} (clear) and SW_{net} for Ohio-Tennessee river basin (left) and transformation to effective cloud albedo (right).

Reflective cloud is well observed from space so this gives us a tool to assess SWCF in our reanalyses, using data sets like the ISCCP data (which also estimate surface albedo). Figure 4 shows such a comparison between ERA-40, ERA-Interim and the ISCCP data for the period 1990-2001 (Betts et al., 2008a). The upper curves are the mean seasonal cycle of α_{cloud}, with the interannual variability shown for ERA-Interim and ISCCP; and the middle curves are the differences ERA-Interim – ISCCP and ERA-Interim – ERA-40, and their interannual variability. The lower curves on the right-hand-scale are α_{surf}; for which the interannual variability is shown only for ISCCP (for which it is unrealistically large). For the Amazon (left panel), α_{cloud} peaks in February in the rainy season and has a minimum in August in the dry season. ERA-40 has more reflective cloud than ISCCP, and ERA-Interim has still more. Note that the variability of the differences between reanalyses and ERA-Interim and data are rather small. There are major changes in the physics between the two reanalyses (cycle 23R4 and 31R2:

see http://www.ecmwf.int/products/data/technical/model_id/index.html).
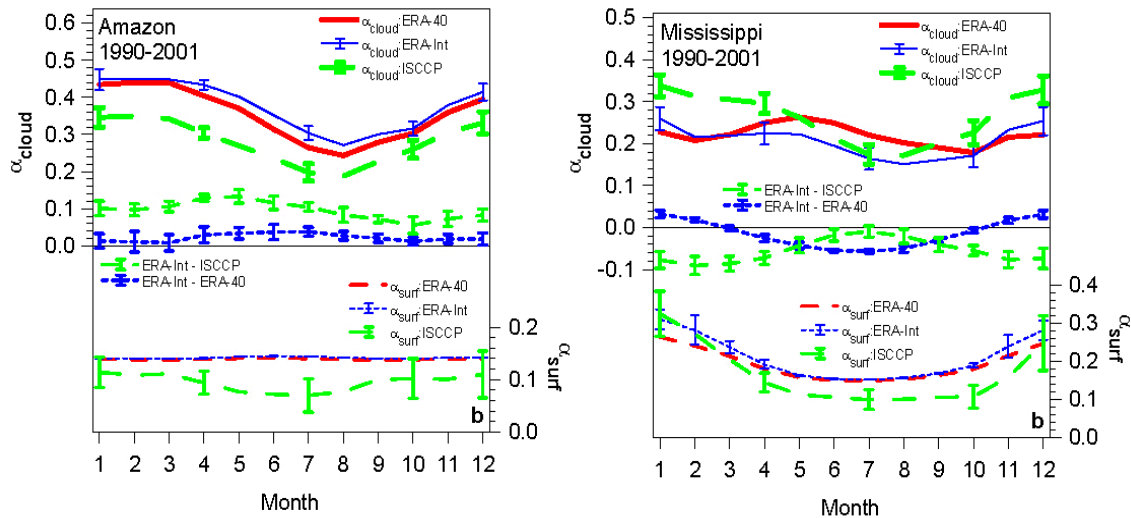
Figure 4: Comparison of annual cycle of α_{cloud} and α_{surf} in ERA-40, ERA-Interim and ISCCP for Amazon and Mississippi river basins.

For the Amazon, ERA-Interim has too much low cloud and a -1.7K cold temperature bias (Betts et al., 2008a). The lower curves for the surface albedo show that the ISCCP estimate is of little value. There are large differences between years and a drop of order 6% in April 1995 (not shown), when the coverage of the Amazon by the geostationary METEOSAT-3 was replaced by a GOES satellite with a rather different radiometer spectral response (Rossow, 2008, personal communication). Zhang et al. (2007), in a detailed comparison, suggests that the uncertainty in surface broadband albedos derived from different global datasets is of order 7%.

For the Mississippi (right panel), the comparison shows a different story. Relative to ISCCP, ERA-40 has a high α_{cloud} bias in summer and a low bias in winter. ERA-Interim has systematically greater α_{cloud} in winter and smaller in summer, so this generally reduces the ERA-Interim bias for this mid-latitude basin. The pattern of change is similar for the Mackenzie basin (not shown). Betts et al. (2006) compare a long time-series of high-quality data at three Boreal Ecosystem Monitoring Study (BERMS) sites in Saskatchewan with ERA-40 data from the nearest grid-point. They show a very similar seasonal pattern in the ERA-40 bias of α_{cloud}, as well as more detail of the daily time-scale; in particular, how cloud biases project onto the SEB.

2.5.   Surface LW$_{net}$

The surface LW$_{net}$ plays a fundamental role in land-atmosphere coupling. The upward and downward LW fluxes are strong functions of temperature. However, on daily-mean timescales, LW$_{net}$ is a strong function of humidity and cloud cover, but weakly dependent of temperature; whenever there is strong vertical coupling of the atmospheric structure, for example by convection within the boundary layer. Figure 5 compares extended summer observations from BERMS of daily-mean LW$_{net}$, binned by near-surface RH and cloud albedo with the nearest grid-point from ERA-40 (Betts et al., 2006). The clear-sky fluxes from ERA-40 are replicated on the left panel for BERMS. The time-periods are not the same, although they overlap; but the statistics of the relationship are identical within the (rather small) standard deviations shown for the variability of the daily data. Outgoing LW$_{net}$ decreases as near-surface RH rises (and mean cloud-base falls), and decreases as cloud cover increases (represented here quantitatively by its scaled SWCF). Here we see conceptually separated, the clear-sky LW greenhouse effect, and the LW cloud forcing, the greenhouse warming from cloud cover. At cold temperatures, when the solar zenith angle is low, such as in winter at high latitudes, the warming from the LWCF dominates over the cooling from the SWCF.
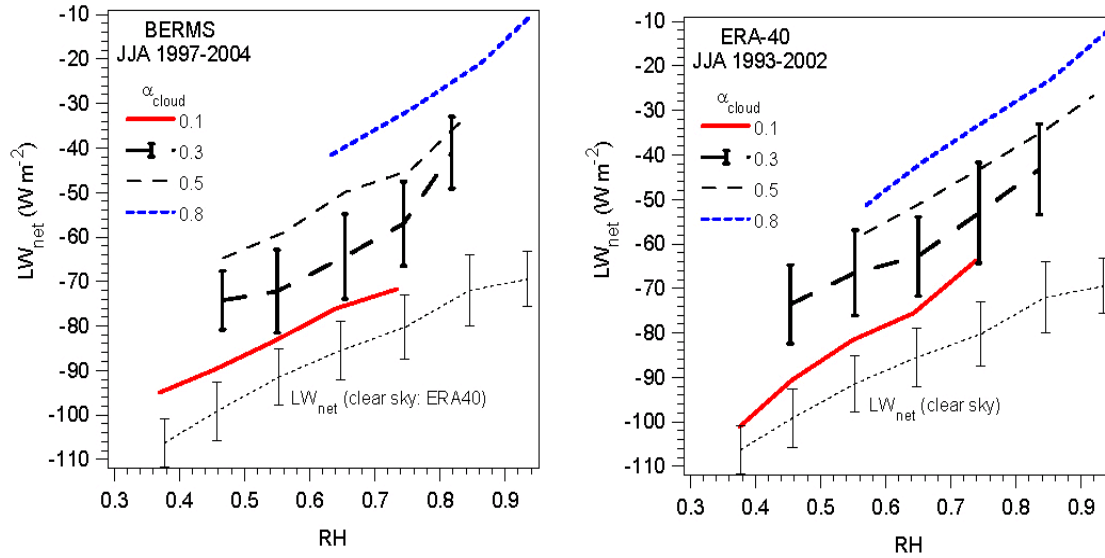
Figure 5: LW_{net} binned by 2-m RH and α_{cloud} for BERMS data and ERA-40 nearest grid point

2.6. Coupling of LW_{net} with diurnal cycle and NBL

In turn LW_{net} plays a fundamental role in the diurnal cycle over land. The strength of the nocturnal BL (NBL) is linked to the cooling from LW_{net}; since the stronger cooling, with a clear dry atmosphere above, gives a lower minimum surface temperature at night. In terms of the daily climate, the strength of the NBL is closely related to the diurnal temperature range, defined as

$$DTR = T_{max} - T_{min} \tag{5}$$

where T_{max}, T_{min} are the maximum and minimum values of 2-m temperature, T_2.

Figure 6, from Betts (2006), illustrates some relationships using ERA-40 data for the Madeira River, a southwestern basin of the Amazon that has a large seasonal cycle of precipitation and humidity. The left panel shows that the mean DTR roughly doubles from the wet season in January and February to the dry season in July and August. For this Amazon basin, sunrise is around 1030 UTC; slightly later in July and August, as the basin is south of the equator. The surface outgoing LW_{net} has a similar increase from wet to dry season (not shown), because in the dry season, the atmospheric water vapor and cloud cover are reduced, and the lifting condensation level (LCL) is higher, and all these factors contribute to a greater outgoing LW_{net}. In fact, ERA-40 shows the same LW_{net} dependencies on humidity and cloud over the Madeira River as in Figure 5 for BERMS (Betts and Viterbo, 2005).

We can define a radiative temperature scale from the LW_{net24}, the daily mean LW_{net}, as

$$\Delta T_R = -\lambda_0 LW_{net24} \tag{6}$$

where $\lambda_0 = 1/(4\sigma T^3)$ is the radiative sensitivity parameter from the differential of the Stefan-Boltzmann law, in which the Stefan-Boltzmann constant $\sigma = 5.67 \, 10^{-8} \, W \, m^{-2} \, K^{-4}$. At $T = 293K$, $4\sigma T^3 = 5.7 \, Wm^{-2} \, K^{-1}$, giving $\lambda_0 = 0.175 \, K/(Wm^{-2})$. We can use ΔT_R to scale the diurnal cycle of temperature, by defining a scaled temperature perturbation from the 24-h mean temperature, T_{24}, as

$$T_{sc} = (T_2 - T_{24}) / \Delta T_R \tag{7}$$

Scaled in this way, the diurnal cycles of temperature collapse into a single curve with an amplitude, $DTR_{sc} = T_{maxsc} - T_{minsc}$, close to unity, shown on the right panel. Betts (2006) show that this scaling can be extended across all latitudes. There is an increase of DTR_{sc} with night-length and a rather weak decrease with the surface wind-stress. The right panel also shows the corresponding diurnal variation of surface heat flux, H, in ERA-40. If we note that the NBL development starts when H changes sign, marked as T_{Nsc}, then we can define the scaled *strength* of the NBL at the sunrise T_{min}, as

$$\Delta T_{Nsc} = T_{Nsc} - T_{minsc} \tag{8}$$

With the surface and BL parameterizations in ERA-40, DTR and NBL strength are closely related across all latitudes with $\Delta T_{Nsc}/DTR_{sc} \approx 0.9 \pm 0.07$ (calculated from river basin daily statistics).

From this daily climate perspective, the daytime and night-time BLs are a fully coupled system. When conditions are dry, surface evaporative fraction is low, H is high and λE is low, giving a deep dry daytime BL with less cloud cover. Outgoing LW_{net} is large and at sunset the surface cools rapidly to a lower T_{min} at sunrise. The temperature rise after sunrise is also rapid, both because H is large, but also because there is a deep residual mixed layer from the previous day. Betts (2003) gives illustrations of this at high latitudes. One of the remarkable aspects of the historical development of theories for the unstable and stable BLs has been the focus on the dynamics, the turbulence; while ignoring the constraints imposed by the driving radiative processes. The introduction of the ML model (e.g. Betts, 1973) refocused our thinking for the daytime BL. Perhaps this radiative scaling (Betts, 2006) will help refocus our understanding of the NBL.
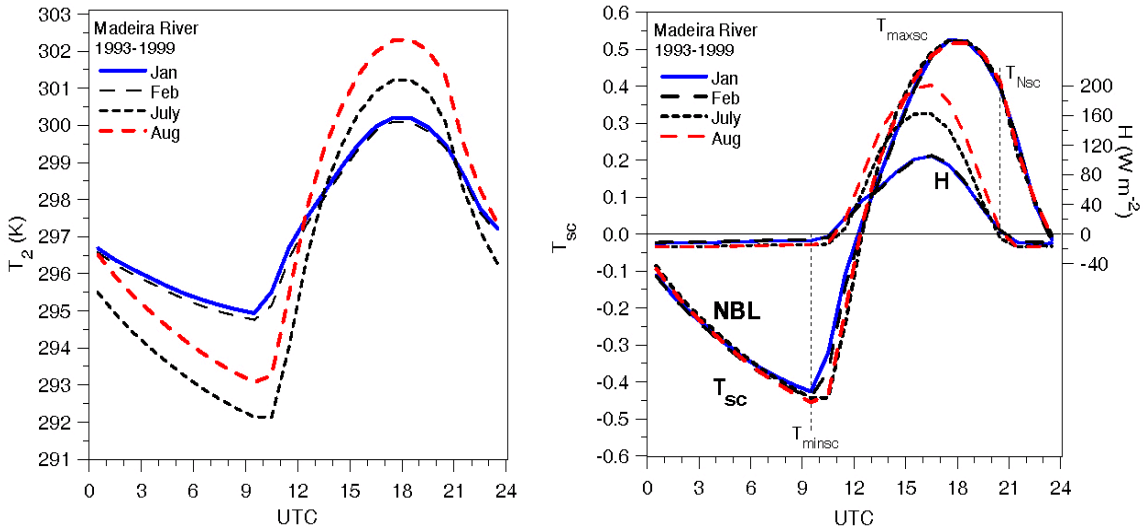

Figure 6: Diurnal cycle of 2-m temperature in ERA-40 for Madeira River basin (left) and (right) surface heat flux and scaled 2-m temperature (Eq. (6)).

3.   Role of water availability and clouds in the surface energy partition

The availability of water for evaporation and transpiration plays a fundamental role in the SEB. Over land, it essentially determines evaporative fraction

$$EF = \lambda E/(\lambda E+H) \tag{9}$$

This is one of the basic differences between land and ocean: the other being the large difference in thermal capacity between the land-surface and the ocean mixed layer. Clouds on the other hand have a large impact on the surface radiative fluxes.

Figure 7 illustrates the role of primarily soil water in the surface energy partition, and the impact on the diurnal cycle of 2-m temperature and humidity. Twenty-eight days with nearly clear skies during July and August, from the 1987 FIFE grassland prairie experiment near Manhattan, Kansas (Betts and Ball, 1995, 1998) have been stratified into three roughly equal groups, based on the 0-10cm volumetric soil moisture (which was measured gravimetrically). The left panel shows the mean diurnal cycle of R_{net} (left-hand-scale) and daytime evaporative fraction EF (right-hand-scale). R_{net} is almost the same for each group of days, peaking around 615 W m^{-2} at local noon (about 1820 UTC), because they were chosen for nearly clear skies. However the partition of R_{net} into λE and H, represented by EF is radically different. As mean soil moisture increases from 14.7% (when the vegetation is stressed) to 29.9% (when the vegetation is unstressed), near-noon EF increases from 0.54 to 0.75. The right panel shows the large impact of these different surface fluxes on the diurnal cycle of 2-m temperature, T, and relative humidity, RH. We see the typical mirror opposites of RH falling as T rises (because diurnal changes of mixing ratio are relatively small) for all the data. However, with drier soils, there is a systematic shift to higher temperature and lower RH.
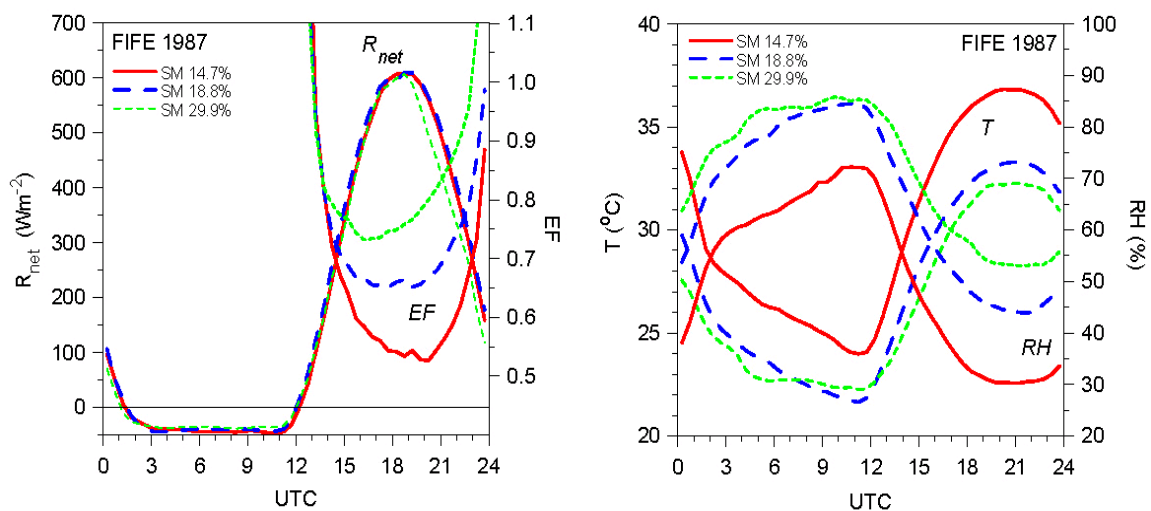

Figure 7: Diurnal cycle of R_{net} and EF (left) and 2-m temperature and RH (right) for FIFE summer composites

From wet to dry soils, the afternoon RH minimum drops from 53% to 30%. This corresponds to an increase in P_{LCL}, the pressure height of the LCL above the surface, from 134 to 239 hPa in the afternoon. I use P_{LCL} extensively as measure of the LCL, because it can be computed easily from parcel T and pressure p, as

$$P_{LCL} = p - p* \tag{10}$$

where p* is the parcel *saturation pressure*: the pressure at the LCL, when a parcel lifted dry adiabatically reaches water vapour saturation. Saturation temperature and pressure (T*, p*) define the properties conserved in reversible adiabatic processes (Betts, 1982), and the properties of parcels as they cross cloud boundaries. Over land, when there are BL clouds in the afternoon, P_{LCL} gives a good estimate of mixed layer depth.

3.1.   Aside on the relation of RH to LCL

The thermodynamic relation of Z_{LCL} (the height of the LCL) and P_{LCL} as a function of parcel T, RH and pressure, P, is summarized in Figure 8. The left panel shows Z_{LCL} as a function of temperature (the dependence on pressure is negligible in the lower troposphere), and the right panel shows that the ratio P_{LCL}/p has only a weak dependence of T. So the relative humidity and the pressure height of mean cloud-base are very closely linked.
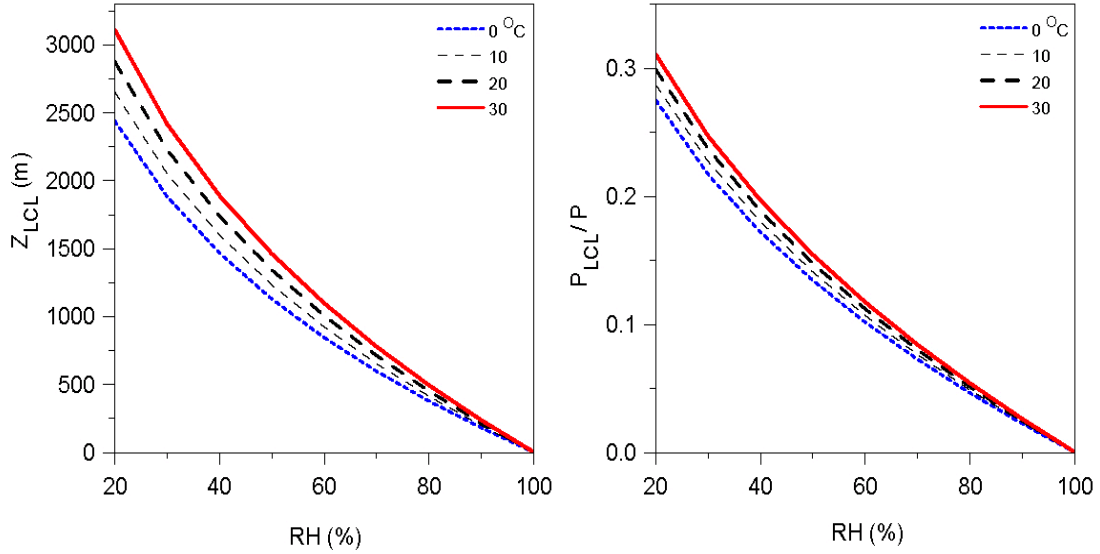
Figure 8: Relation between RH and Z_{LCL} and P_{LCL} as a function of parcel T, p

3.2. Diurnal cycle on vector diagrams

Vector plots are helpful for visualizing the balance of processes involved in the diurnal cycle (Betts, 1992). Figure 9 is a remapping of the daytime 2-m diurnal cycle (from 1115 to 2245 UTC) of the three FIFE soil moisture composites in Figure 7 into a conserved parameter reference frame. The left panel is a (θ, Q) plot (potential temperature and mixing ratio): with a duplicate $(C_p\theta, \lambda Q)$ scale in J kg^{-1}. The right panel is the same data on a (θ_E, P_{LCL}) plot (equivalent potential temperature, pressure height to LCL). The left panel has auxiliary dotted lines, corresponding to saturation pressure, p* = 900hPa, and virtual potential temperature, θ_v = 298K. We also show a schematic vector budget for the BL budget from 1415 to 2045 as heavy solid and dashed lines (Betts, 1992). The simplified mixed layer (ML) budget can be written for a time-step, Δt, when the mean depth of the mixed layer is ΔZ_i, as

$$\Delta \boldsymbol{\xi_m}/\Delta t = (F_s - F_i)/ \rho\Delta Z_i \tag{11}$$

where $\Delta \boldsymbol{\xi_m} = \Delta(C_p\theta, \lambda Q)_m$ is the change in ML values over the time-step, which we will approximate with the change in 2-m values of $(C_p\theta, \lambda Q)$ between 1415 and 2045. The surface fluxes are the heavy solid line, calculated as [setting $\theta/T \approx 1$]

$$(H, \lambda E) = \Omega \, \Delta(C_p\theta, \lambda Q) \tag{12}$$

using the scaling

$$\Omega = \rho\Delta Z_i/\Delta t \tag{13}$$

The ML step from 1415 to 2045 can then be regarded as the sum of the surface flux vector and the entrainment vector (heavy dashed). So as a residual, this gives an estimate of the entrainment fluxes into the growing ML, using (13). Note that it is a vector that warms and dries the ML. We have of course ignored advection in the simplified Eq (11), so the advection of $(C_p\theta, \lambda Q)$ in time Δt is also a vector contribution to this residual. Warm, dry advection will have a similar impact on the ML as the entrainment of warm, dry air from above. Using a large time-step (here 6.5h) in (11) introduces a small approximation, but for the case shown it is only a few %.
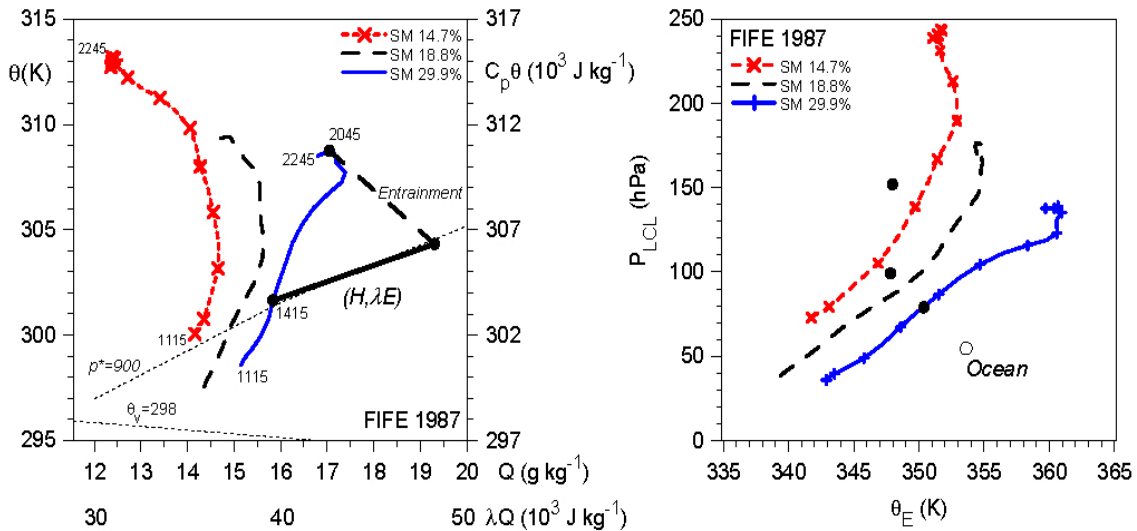
Figure 9: Daytime 2-m diurnal cycle for three FIFE composites, partition by soil moisture: (left) a (θ, Q) plot, showing vector budget from 1415 to 2045 UTC, and (right) a (θ$_E$, P$_{LCL}$) plot

The slope of the surface flux vector on this figure is related to the surface Bowen ratio, BR = H/λE: it is actually (θ/T)(H/λE), since the figure is plotted in terms of potential temperature. For this high soil moisture case, the surface flux vector is slightly less than the slope of p* = 900 hPa, meaning that the surface fluxes alone would tend to lower cloud-base. It is the entrainment fluxes that are responsible for the rise of cloud-base. For this high soil moisture composite, we have an estimate of mixed layer depth, ΔZ$_i$(t), from sequential sondes (Betts and Ball, 1994), launched during intensive periods. We do not show the corresponding vector figures for the drier soils, because there is no sonde data. However as EF falls, BR increases and the surface flux vector becomes steeper (that is it rotates anti-clockwise), which contributes to the greater rise of P$_{LCL}$. In addition, entrainment of dry air from above the ML (which has a lower saturation pressure) also increases as H increases.

The right panel showing (θ$_E$, P$_{LCL}$) gives a reference for moist processes. Also shown (open circle) is the equilibrium state over a tropical ocean corresponding to the same daily mean surface flux, H+λE, as our FIFE composites, from the solutions of Betts and Ridgway (1989); and the 24-h mean surface 2-m states for our FIFE composites (solid circles). The picture here is that, although the mean state over land has a lower θ$_E$ than over the oceans, the superimposed diurnal cycle over land gives a higher θ$_E$ in the afternoon; and the highest values (favoring deep convection) for the wettest soils for which evaporation is the highest. Afternoon cloud-base is the lowest over wet soils, although not as low as over the ocean.

3.3. Water availability, Evaporation and LCL

The fundamental reason why the LCL is higher over land than over the ocean is that water is less available for evaporation. In physiological terms the resistance to transpiration means there is a drop in the RH across a leaf. In Figure 7, differences in soil moisture for this grassland prairie change the EF, and the diurnal cycle of RH with corresponding differences in the diurnal rise in the LCL. Model parameterizations, which link evapotranspiration to soil moisture, reproduce this behaviour in the land-surface climate.

Figure 10 (left panel) shows the warm season diurnal cycle in ERA-15; an average over the Missouri river basin binned in 2% ranges of 0-7cm soil moisture. The four soil-layer land-surface model at that time was Viterbo and Beljaars (1995). There is a monotonic increase in P$_{LCL}$ (with a corresponding decrease in RH) for drier soils. This is characteristic of this type of land-surface model, although it is an over-simplified

representation. For example, over the boreal forest with extensive regions of wet organic soils, soil moisture is a much weaker control on EF and LCL. However, there are extensive moss layers on the surface in spruce forests, which store substantial water after rain (in addition to the water storage in the canopy). After heavy rain, evaporation falls on sequential days as this surface vegetation layer dries out. The right panel shows the diurnal cycle of P_{LCL} in summer for the BOREAS northern study site. The data has been binned by a *wet surface index*, based on recent past rainfall (Betts et al., 2001b). For an index of 5, which means more than 5mm of rain fell the previous day, LCL is low. After five days without rainfall, an index of zero, afternoon P_{LCL} has increased from 75 to 195 hPa.
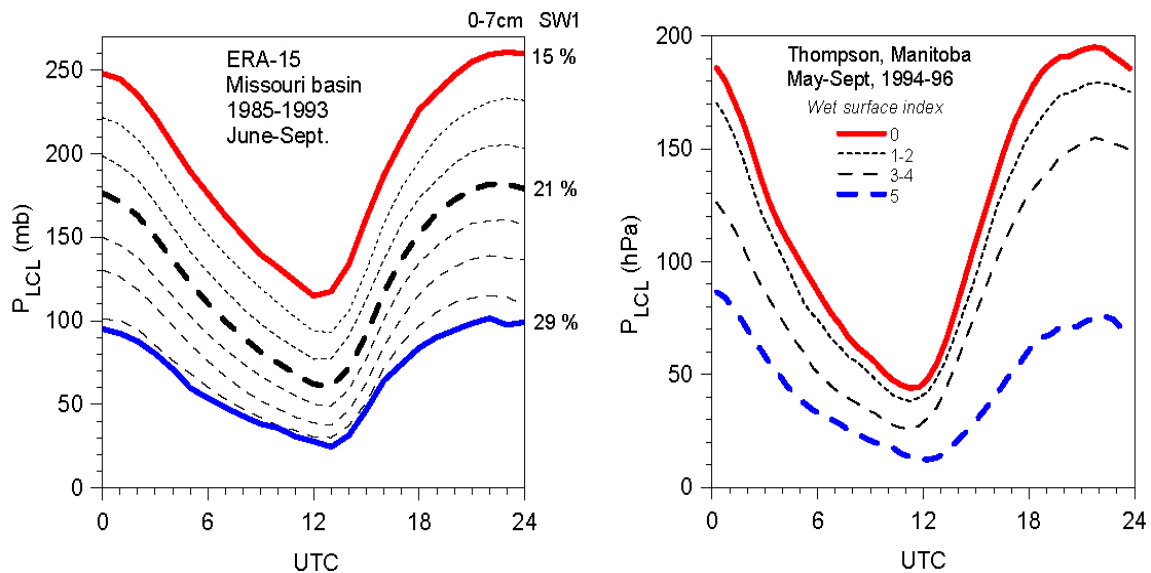

Figure 10: Warm season diurnal cycle of P_{LCL} for the Missouri river basin as a function of 0-7cm soil moisture (left) and (right) for boreal forest site in Thompson, Manitoba

RH is a routine measurement (although accurate measurement is often a challenge) and P_{LCL} can be calculated from p, T and RH (and when BL clouds are present, lidar ceilometers give an independent measure of LCL). So we can think of P_{LCL} as an *observable,* linked to the availability of water for evaporation, which can be used to evaluate the impact of model parameterizations on surface climate in the model.

3.4.   Land-surface-BL Coupling

In the coupled land-surface-BL system, evapotranspiration is just one factor. We see in Figure 10 that the 24-h mean P_{LCL} shifts with the availability of water for evaporation, so it is useful to look at the relationships between daily mean parameters. The BL equilibrium of RH and LCL on daily timescales depends on atmospheric processes as well as surface processes.

Figure 11 shows for ERA-40 for the Madeira river the joint dependence of P_{LCL} (with RH plotted on right-hand-scale with slight approximation) binned by precipitation rate (in mm day^{-1}) and first-layer soil moisture index, SMI-L1 (left panel) and EF (right panel). SMI-L1 is computed for the first 0-7cm soil layer as

$$SMI\text{-}L1 = (SM\text{-} 0.171)/(0.323\text{-}0.171) \tag{14}$$

where SM is the model soil water fraction, the model soil permanent wilting point is 0.171 and the model field capacity is 0.323. SMI-L1 is not only a useful index on the daily time-scale for the availability of water for evaporation (although transpiration depends also on soil water in deeper layers), but it also responds to precipitation on this time-scale. A representative set of standard deviations of the daily mean data are shown.

Not surprisingly as SMI and EF increases, mean cloud base descends and RH increases; but RH also increases as precipitation increases. This is a highly coupled system. When the LCL is lower, more precipitation is likely; but the converse is also true: the evaporation of precipitation as it falls through the sub-cloud layer will lower the LCL, and increase SMI-L1 on daily time-scales.
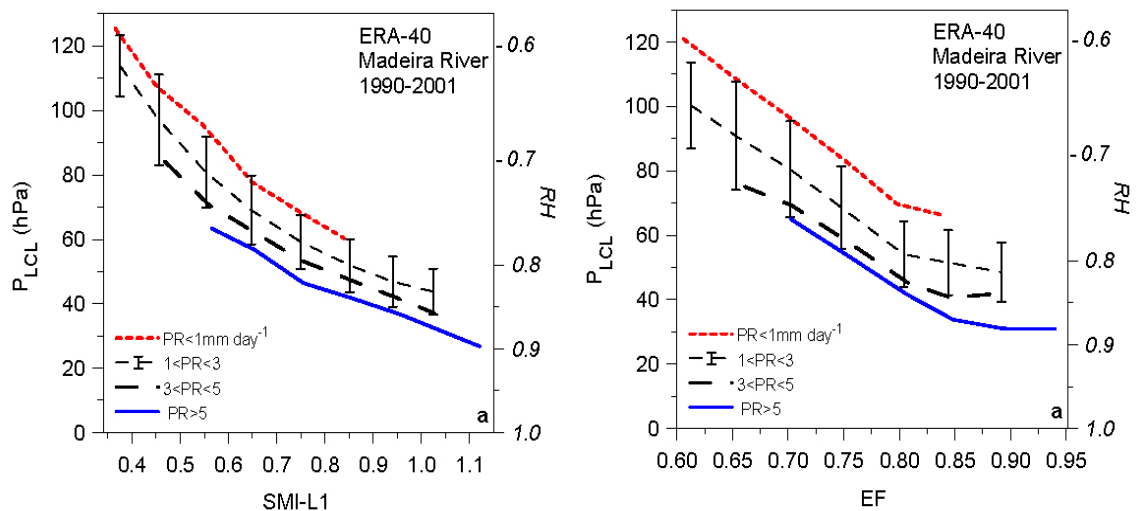

Figure 11: Stratification of P_{LCL} by soil moisture index and precipitation (left) and (right) EF and precipitation. Daily-mean ERA-40 data for Madeira River

Figure 11 links one key *observable* (P_{LCL}) with several important but poorly measured processes in the land-surface-atmosphere coupling. Over the diurnal cycle of the boundary layer the atmosphere integrates over much larger spatial scales, so that the diurnal cycle of P_{LCL} and its daily mean represent processes on scales of order one day's advection (432 km at 5 m s^{-1}). Soil moisture is an important parameter in the model system, but in the real world, in-situ measurements of soil moisture represent quite local processes. Satellite microwave measurements may give us useful estimates of near-surface soil moisture. EF can be measured on towers, but these are representative only of a local footprint. On basin-scales we can make estimates of the land-surface fluxes using hydrologic models (Maurer et al., 2002). Evaporation of falling precipitation plays a fundamental role in the model surface interaction, because evaporation of water above the surface cools and moistens the BL, which increases the surface Bowen ratio; while evaporation off a wet canopy reduces the Bowen ratio. The structure shown in Figure 11 for ERA-40 is broadly consistent with observations, but models in general show a wide range of behaviour (Dirmeyer et al., 2006).

3.5.   Separating cloud and surface controls on the SEB and EF

Figure 12 gives a conceptual split of the surface energy balance in terms of the atmospheric and cloud processes that primarily determine R_{net}; and the surface processes, soil moisture and temperature that primarily determine EF (the partition of R_{net}). We use ERA-40 data, averaged over the Missouri river basin (Betts, 2007), so the figures reflect the physical parameterizations in that reanalysis.

The left panel is the partition of R_{net} into the clear-sky $R_{net}(clear)$ and the cloud forcing CF = SWCF + LWCF.

$$R_{net} = R_{net}(clear) + CF \qquad (15)$$

We have chosen May-August, so the variations in the TOA solar flux are small. We have added the partition with soil moisture, SMI-L1, but this has no impact on CF, which depends almost solely on α_{cloud} (see (3) and Figure 5). $R_{net}(clear)$ also has little dependence on SMI-L1. Surface albedo, not shown, has little variability

in summer. So we can think of surface R_{net} being the sum of the clear-sky flux with little variability in summer and the atmospheric cloud forcing, which has a linear dependence on α_{cloud}.
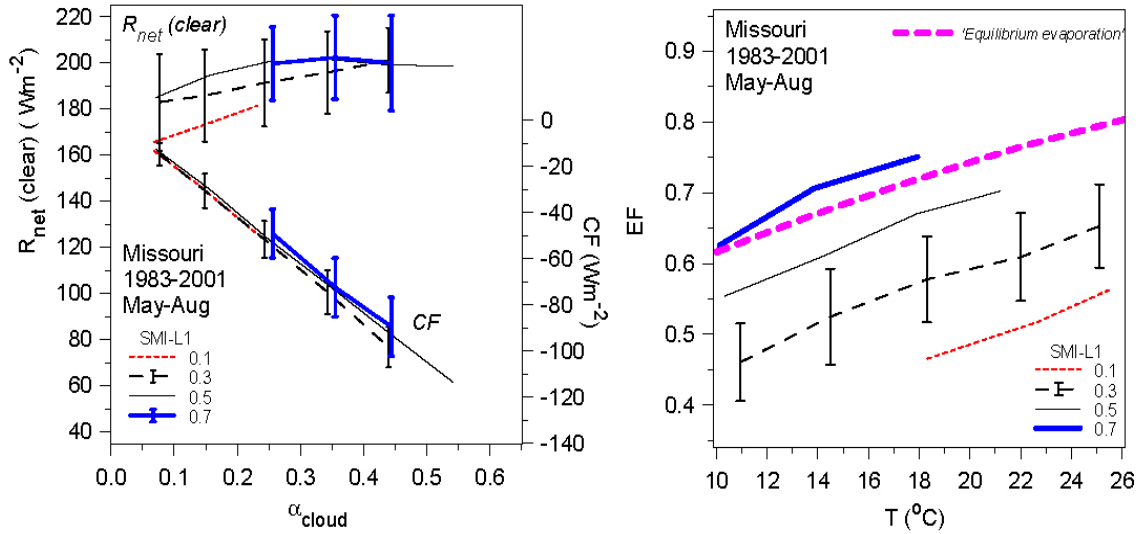

Figure 12: Dependence of R_{net} (clear-sky) and cloud forcing on α_{cloud} (left) and (right) EF on temperature and soil moisture index.

EF shown in the right panel determines the partition of R_{net}; and this is a strong function of soil moisture, represented here by SMI-L1, but also of temperature. The slope with temperature is close to the slope of the classic 'equilibrium evaporation' relation [*Priestley and Taylor* 1972; *McNaughton* 1976], defined as

$$EF^* = \beta/(1+\beta) \qquad (16)$$

where $\beta(T) = (\lambda/C_p) (\partial q_s/\partial T)_p$ is related to the slope of the Clausius-Clapyron equation at constant saturation pressure, plotted here for the mean surface pressure, 900hPa for the Missouri river basin. The slope of the saturation pressure line, $p^* = 900$hPa, in Figure 8 is just $(\theta/T)\beta$. The slope of (16) on Figure 12 just comes from the non-linearity of the Clausius-Clapyron equation. There are of course many other non-linear processes influencing the surface fluxes in the model (ERA-40), but we can loosely interpret the right panel as conceptually splitting the thermodynamic impact of increasing temperature on EF (at constant p^*) from the impact of decreasing soil moisture (and increasing vegetative resistance), which by dropping the RH across the leaf, reduces mixed layer RH and p^*, and increases P_{LCL} and mean cloud-base.

3.6. Coupling between cloud albedo and surface fluxes

Stratifying surface fluxes by cloud albedo changes our perspective on the SEB. Figure 13, adapted from Betts et al. (2006), stratifies surface flux data in summer by cloud albedo; comparing BERMS observations from three forest types, stands of old aspen, black spruce and jack-pine (abbreviated on the Figure as OA,OBS and OJP), with ERA-40 data from the nearest grid-point. On panels (a) and (b) the heavy lines are the ERA-40 data. The left panel (a) shows the radiation fluxes and RH stratified by α_{cloud}. All three flux sites and ERA-40 show a similar structure: quasi-linear behaviour of the net fluxes with α_{cloud}, consistent with our earlier Figure 5 (also BERMS data) and Figure 12 (ERA-40, Missouri basin). The lower surface albedo of the conifer sites give slightly larger net SW fluxes with low cloud cover, but model and observations broadly agree, and show the surface radiation fluxes are largely determined by the surface SW cloud forcing. Note the increase of mean 2-m RH with α_{cloud}.
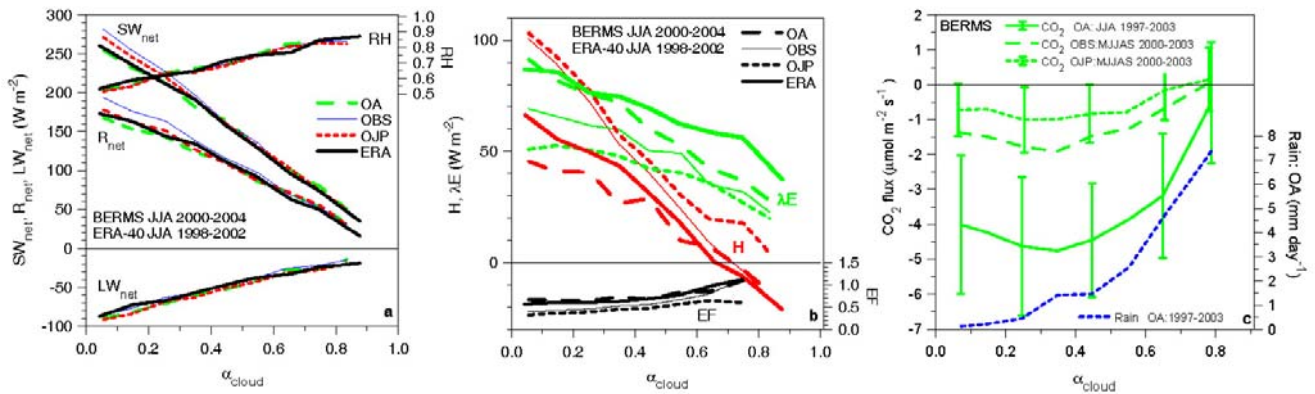
Figure 13: α_{cloud} stratification of (a) radiation fluxes and RH; (b) H, λE and EF; (c) Net CO_2 flux and precipitation

The center panel (b) stratifies H, λE and EF by α_{cloud}. For the conifer sites (the dominant landscape cover) and for ERA-40, the slope of sensible heat flux with α_{cloud} is much steeper than the slope of λE: that is variations in cloud cover and R_{net} are projected more onto H than λE; so that EF increases with reflective cloud cover. For the deciduous aspen site, which has the highest EF in summer, changes in R_{net} from α_{cloud} are projected roughly equally onto H and λE. Traditional hydrologic models link evaporation to R_{net}, but in the fully coupled system, it is H not λE that is more tightly coupled to R_{net} for these conifer sites and in ERA-40 (Betts 2004). In ERA-40, model errors in cloud cover are largely projected onto H (Betts et al. 2006).

The right panel (c) shows the stratification of the net CO_2 flux for the BERMS sites by α_{cloud}, and the corresponding distribution of mean precipitation for the aspen site (point precipitation is a noisy field and the standard deviations, which we do not show, are as large as the mean). All the BERMS sites show a weak maximum in their net ecosystem exchange at an intermediate $\alpha_{cloud} \approx 0.35$, characteristic of a typical cumulus cloud fraction. This is probably due to a combination of factors: vapor pressure deficit stress under clear skies and the higher photosynthetic efficiency for diffuse radiation (scattered by the cloud field). Clearly there are many processes involved in the coupled system, and many need further study.

4. Feedbacks to larger scales

4.1. Evaporation-precipitation feedback

One of the fundamental issues in the land-surface-atmosphere coupling is the strength of evaporation-precipitation feedback, referred to in the introduction. There have been many attempts to quantify this statistically using models (see Koster et al., 2006), but it is has been hard to evaluate against observations, because there are no routine measurements for the central links in the chain, soil moisture and EF, that are representative of the grid-scale. There have been many model sensitivity experiments. Figure 14 shows an example from Beljaars et al. (1996) of continental-scale evaporation-precipitation feedback. The great flood on the Mississippi of July 1993 occurred in the same month that ECMWF was running in parallel the new land-surface model of Viterbo and Beljaars (1995) with four soil layers to better represent soil moisture memory on different timescales. This model had been tested off-line with the land-surface and soil moisture data from the 1987 FIFE experiment (Betts and Ball, 1995), as well as other data sets. The 3-day forecasts with the new four soil layer model were much better for the July 1993 rainfall than the old 2-layer model. We had also seen considerable sensitivity in idealized seasonal soil moisture experiments. Forecasts starting in May with wet or dry soils showed a significant positive feedback on precipitation through-out the summer. So we ran soil moisture sensitivity experiments for July, 1993. Figure 14 shows the difference in the total July precipitation between forecasts starting with "wet" or "dry" initial soil conditions on July 1, 2 and 3 (see

Beljaars et al. (1996) for details). There is a broad maximum over 4mm day^{-1} (red shaded contours), corresponding to >120mm for the month, located near the observed precipitation maximum over the central US. It is clear that the positive feedback on precipitation is large in the model if the soil is initially wet; and this positive signal can be seen over most of the continental US. One difference we noticed was that cloud-base was much lower over initially wet soils: the link seen in Figure 11. However, increased clouds over wet soils reduced surface R_{net}, the source term for θ_E, so that unlike Figure 9 (where R_{net} was the same for wet and dry composites), the wet soil forecasts had lower P_{LCL} but did not have systematically higher θ_E. A lower cloud-base with the same θ_E has a higher saturation mixing ratio, which contributes to greater precipitation.
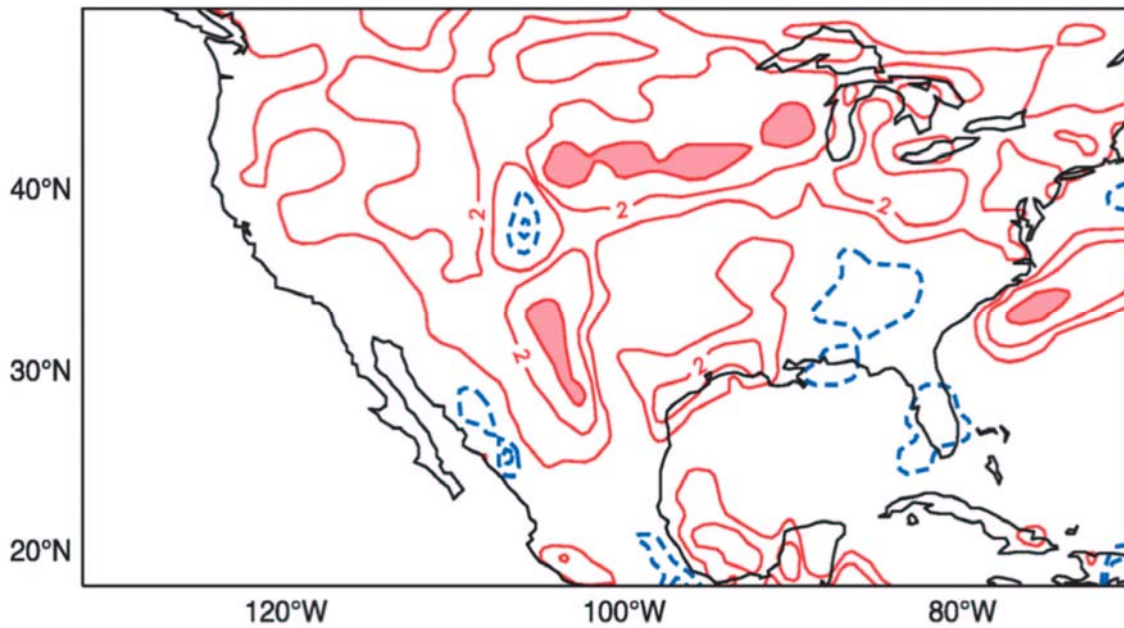

Figure 14: Figure 14. Difference in the 30-day precipitation between two ensembles of three T-106 forecasts starting with Awet@ or Adry@ initial soil conditions on July 1, 2, 3 (Beljaars et al., 1996). Contours are at 1, 2, 4 mm day-1, with the +4 contour shaded red.
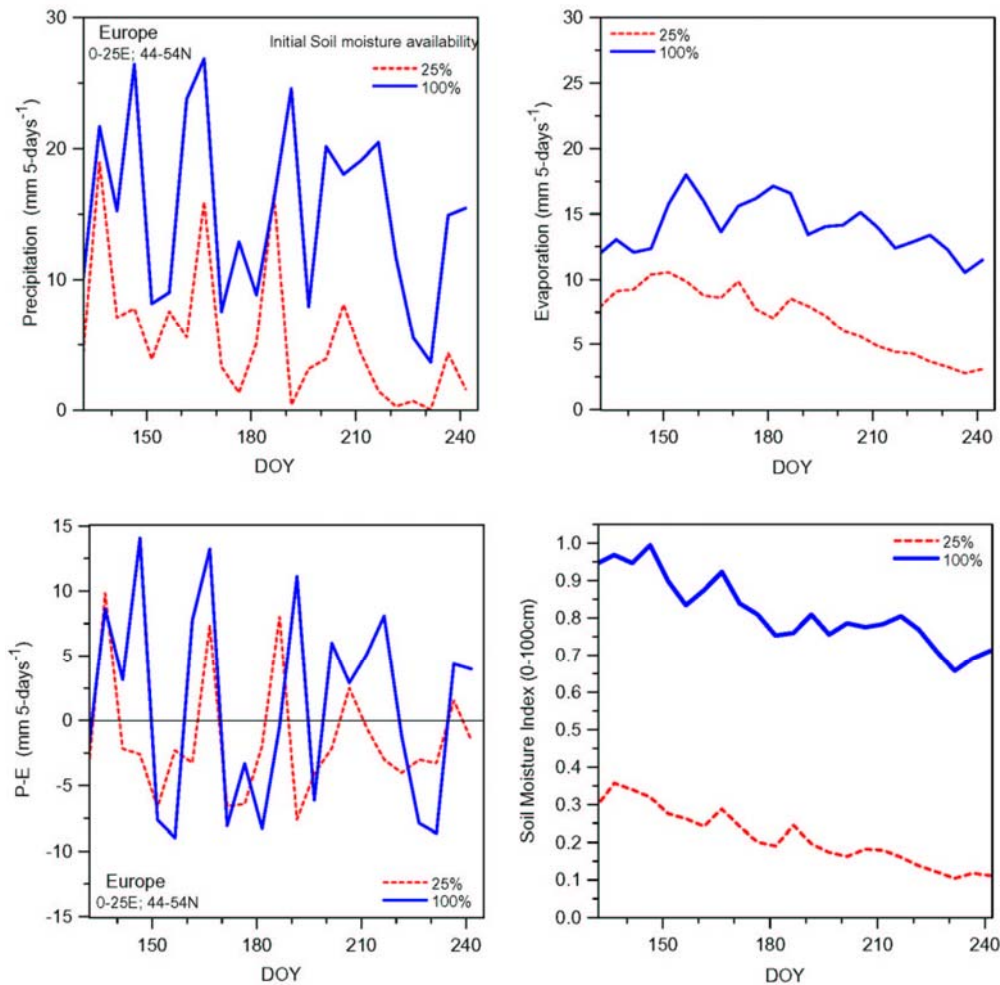
Figure 15. Precipitation, P; evaporation, E; difference, (P-E); and soil moisture index for Europe from two 120-day forecasts from May 1, 1987, starting with initial soil moisture availability of 100% and 25% for vegetated areas.

Betts (2004) revisited this issue with the model used for the ERA40 reanalysis, run at a resolution of T-95 L60. This has a more recent land surface model, including a distribution of vegetation types (Van den Hurk et al., 2000), and other revisions to the physics. Two 120-day forecasts were run from May 1, 1987 with identical sea surface temperatures and initial conditions, except for initial soil moisture. The "wet" forecast has soil moisture initialized at 100% of field capacity for vegetated areas, and the "dry" forecast is initialized with soil moisture at 25% of "soil moisture availability" for vegetated areas. This corresponds to soil moisture indices (see Eq. 14) of 1 and 0.25 for the 0-100cm layer for vegetated areas. Five-day means were extracted for different regions of the globe. Figure 15, an average for Europe from 44-54°N and 0-25°E, shows precipitation, P, evaporation, E, the difference of (P-E), which is a measure of the atmospheric convergence of water vapor, and a soil moisture index. The first 5 days of each forecast is omitted (DOY denotes day-of-year). The memory of the initial soil moisture is retained throughout the summer dry-down for precipitation and evaporation. Precipitation and vapor convergence (P-E) show large synoptic variability. For the forecast initialized with dry soils, the synoptic variability remains, but mean summer evaporation is reduced from 13.9 to 7 mm 5-day^{-1}, and mean precipitation is reduced from 15.5 to 6 mm 5-day^{-1}. Mean P-E, a measure of the atmospheric convergence of water vapor, remains small; although there is a small shift for the summer from 1.6 mm 5-day^{-1} convergence with wet soils to a divergence of -1.1 mm 5-day^{-1} for dry soils. These wet and dry soil seasonal forecasts have of course somewhat extreme initial conditions, but the behaviour is a characteristic of the relatively strong evaporation-precipitation feedback in the ECMWF

model. However, we do not know how accurate it is quatitatively. Nonetheless, land-atmosphere coupling is believed to have played an important role in European heat waves (Fischer et al., 2007), and it is important issue for assessment of changes in surface hydrometeorology as the global climate warms (see Seneviratne et al., 2006).

4.2.   Precipitation and cloud coupling to vertical motion

The Amazon provides a good illustration of the coupling of precipitation, atmospheric structure and cloud cover to the larger-scale dynamics. This is a region where the variation of evaporation is much smaller than N. America, because the deep-rooted forest has access to soilwater through extended dry seasons. The tropical forest in fact has much deeper rooting (Von Randow et al., 2006; Betts et al., 2008b) than ERA-40, but we will use ERA-40 data for illustration, because the data is self-consistent and complete.

Figure 16 plots daily mean ERA-40 data, averaged over the Madeira river basin in the SW Amazon (derived from hourly basin means: see Betts and Viterbo, 2005). The x-axis is mid-tropospheric vertical velocity in pressure co-ordinates, Ω_{mid} (averaged from the hourly data and then over model levels in the middle troposphere, corresponding roughly to the layer between 300 and 700 hPa). The Madeira river basin has a large annual cycle between the wet season in December to March and the dry season in July and August (e.g. see Figures 4 and 6); and the plot shows 12 years of daily means. The left panel shows that on the daily timescale, both total column water vapour, TCWV, and cloud albedo increase non-linearly as mid-tropospheric ascent (Ω_{mid} negative) increases. This is not surprising: low-level convergence and ascent produces moistening and more clouds. This means there is strong coupling between the shortwave and longwave SEB and Ω_{mid}.

The right panel plots daily precipitation and evaporation against Ω_{mid}. Evaporation has little variability when compared to precipitation. To the left, at high cloud cover and large precipitation, a small reduction in E can be seen. Even though ERA-40 probably has more variation of E over the annual cycle than observations, because it has no very deep rooting (the fourth soil layer with some roots extends only to 2.89m), the spread of E with mid-troposphere omega is not large. In contrast, precipitation, P, is essentially linearly related to Ω_{mid} : the red line is the fit $-0.11(\Omega_{mid}-40)$, which goes to zero with $\Omega_{mid} = 40$ hPa day^{-1}, a typical radiatively-driven mid-tropospheric subsidence in the tropics (Betts and Ridgway, 1989). Betts and Viterbo (2005) give a second linear fit to the precipitation $-TCWV(\Omega_{mid}-40)/420$: an estimate of the lower tropospheric moisture convergence.
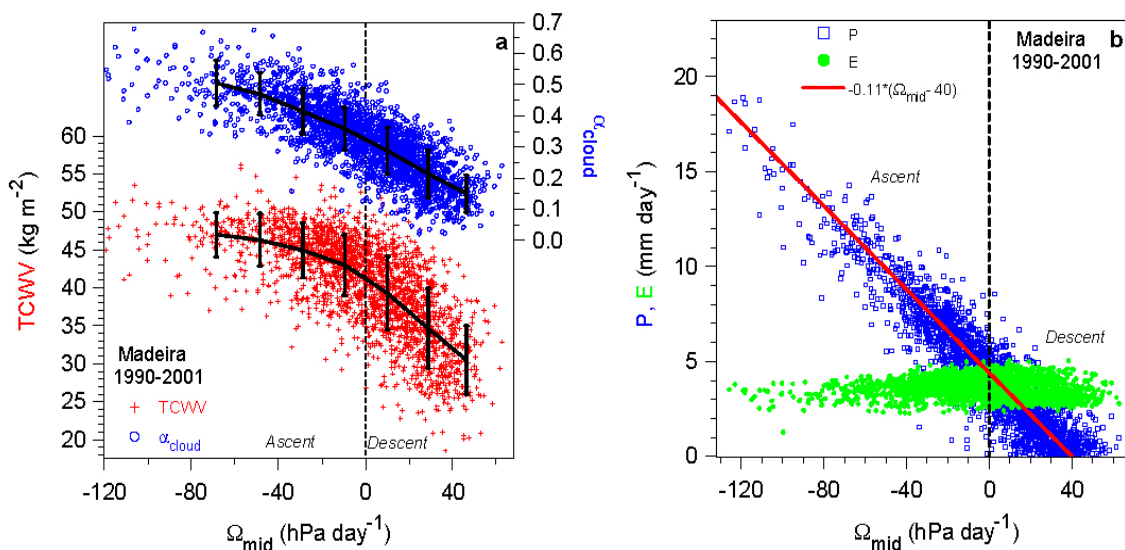

Figure 16: *Daily mean total column water vapour and cloud albedo as a function of omega (left) and (right) precipitation and evaporation for the Madeira river basin*

There is scatter in these daily data, as there are substantial local changes from day-today as well as advection of clouds from other regions of the Amazon. We are also seeing the whole annual cycle: ascent dominates in the rainy season and descent in the dry season (e.g. Betts et al., 2008b). From a climate perspective, we see conceptually in Figure 16 the partition of moisture convergence into moisture storage, cloud cover and precipitation. Now α_{cloud} is a measure of SWCF, the diabatic SW impact of clouds at the surface; and surface precipitation is the diabatic heating of the atmosphere, so their relationship reflects a fundamental energy partition by the model system parameterizations (Betts, 2007; Betts et al., 2008a). We know from Figure 4 that both ERA-40 and ERA-Interim have too much reflective cloud (in comparison to the ISCCP observations), and Betts et al. (2008a) show that both reanalyses have a low bias of precipitation in the rainy season and a high bias in the dry season for the Amazon as a whole. What is needed for every model cycle is an analysis of these relationships for both wet and dry seasons (or disturbed and suppressed conditions) against observations for tropical and mid-latitude climate regimes; as a tool to evaluate model developments.

4.3. Relation of cloud SW forcing to precipitation forcing

For the Mississippi basin, we have data good enough to assess the relation between the surface SWCF and the diabatic forcing of the atmosphere by precipitation. Figure 17 for the Missouri river basin, from Betts (2007), bins 19 years of daily mean warm season precipitation by α_{cloud} (scaled SWCF given by (3)) and P_{LCL}. The left panel is from ERA-40 and the right uses α_{cloud} from ISCCP and gridded precipitation from the Higgins et al (2000) datasets. ERA-40 P_{LCL} has been used to stratify both, because it is somewhat constrained by a surface humidity analysis. For a given cloud albedo, ERA-40 has more precipitation. Converting precipitation to energy units, the ratio of the SWCF to the diabatic precipitation forcing is 0.48 for ERA-40 and 0.74 for the observations for $P_{LCL} = 60$ hPa (Betts, 2007). From a climate perspective this is a large difference in the impact of clouds on the energy partition between atmosphere and the surface. Note that in the observations the radiative impact of clouds and their diabatic impact from precipitation are comparable in magnitude. This is generally true on all timescales in the atmosphere; and it means that the radiation field plays a tightly coupled role in the vertical transports by the cloud field. Often, however, this coupling is not properly represented in models.
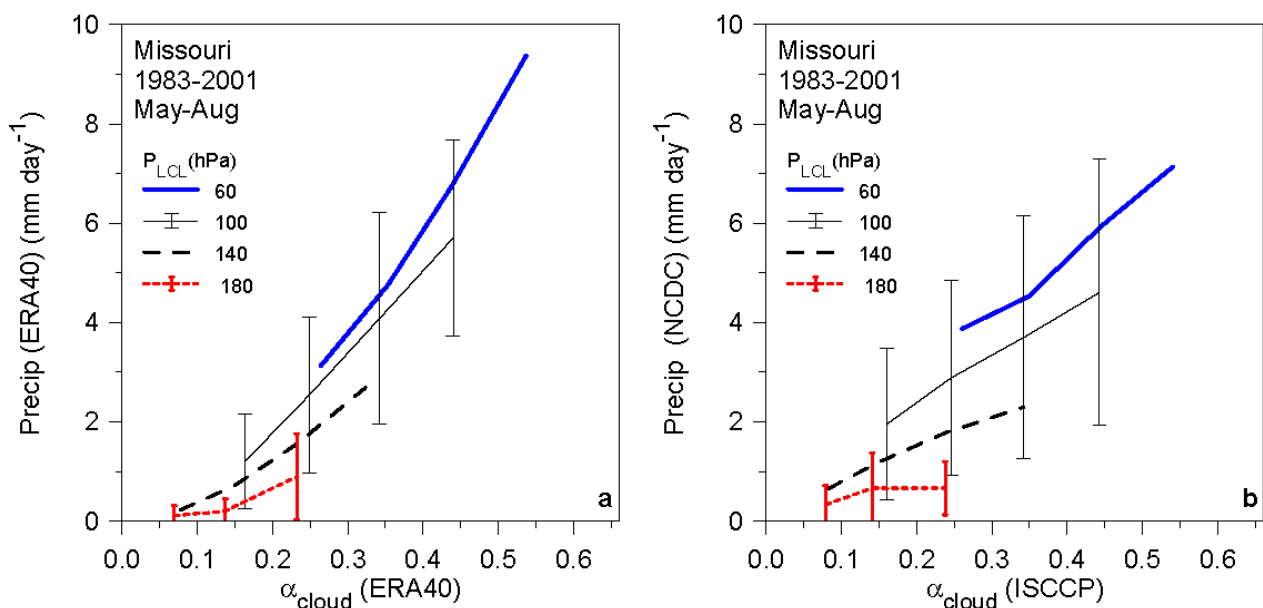

Figure 17: Warm season precipitation for the Missouri river basin stratified by α_{cloud} and P_{LCL} for (a) ERA-40 and (b) NCDC and ISCCP observations

5.   Summary

I have illustrated some of the basic physical processes and links that can be seen in observations and models at the land-surface, using figures selected from papers from the past fifteen years. My framework is both diagrammatic and conceptual; looking for relationships and information in the coupling of processes and observables. Models have only limited value if we do not have a deep understanding of the coupling of processes within model system; and observations are important both for evaluation, and to suggest important processes that are simply missing.

The starting point in section 2 was the surface energy balance and the factors that influence net radiation and its partition into the sensible and latent heat fluxes. The net short-wave was presented as a modification of the incoming surface clear-sky flux by the surface albedo and an effective cloud albedo (the surface shortwave cloud forcing scaled by the clear-sky flux). The land-surface climate depends critically on the accuracy of these two albedos. The net surface long-wave flux is primarily a function of RH and cloud cover. We then drew attention to the role of the net long-wave flux in the diurnal temperature range and the strength of the night-time BL. In section 3, we addressed the role of water availability and clouds in the surface energy partition. We looked at the role of soil moisture in determining EF and the diurnal cycle of temperature, RH and LCL, using grassland data from FIFE. Vector diagrams were presented as a way of visualizing the balance of processes in the time evolution of the daytime BL. We touched on the role of surface and atmospheric processes in determining BL equilibrium, specifically the pressure-height of the LCL; and how, in the surface energy balance, R_{net} variability is dominated by cloud albedo, but EF is largely a function of temperature and soil moisture. Then we looked at how the stratification of the surface fluxes by the cloud albedo further shifts our understanding of the surface energy balance partition. In section 4, we looked at larger-scale issues: the role of soil moisture in evaporation-precipitation feedback in the ECMWF model; and the coupling of mid-tropospheric omega to column water vapor, cloud albedo and precipitation. From a climate perspective, this describes the partition of moisture convergence into moisture storage, cloud cover and precipitation. Finally we looked at the relation of cloud albedo (the scaled surface shortwave cloud forcing) to the diabatic precipitation forcing of the troposphere in ERA-40 and observations; and noted the bias in ERA-40.

What is needed for every model cycle is an analysis of these many relationships, diurnal, daily mean and seasonal for both wet and dry seasons (or disturbed and suppressed conditions) against observations for tropical and mid-latitude climate regimes; as a tool to evaluate model developments. This is a challenge; but it is becoming tractable as both global datasets and point time-series datasets improve. The ERA-40 comparison with BERMS in Betts et al. (2006) is an illustration of this.

There are many issues that have not been covered (including any discussion of vegetation and soil hydrology, the impact of diffuse radiation on forests, the coupling between aerosols, radiation and cloud microphysics and many more. Much more needs to be done to understand the coupling between local processes and the larger scale dynamics, especially for important atmospheric regimes such as the Amazon (eg Betts and Viterbo, 2005) and the monsoon circulations. But it must be clear that the accuracy of the model representation of surface, BL and cloud processes, and the relation between cloud and precipitation processes, is critical for the interaction between scales and in determining the model climate.

References

Beljaars, A.C.M., P. Viterbo, M.J. Miller and A.K. Betts, 1996: The anomalous rainfall over the United States during July 1993: sensitivity to land surface parameterization and soil moisture anomalies. *Mon. Wea. Rev.*, **124**, 362-383.

Betts, A. K., 1973: Non-Precipitating Convection and Its Parameterization. *Quart. J. Roy. Meteor. Soc.*, **99**, 178-196.

Betts, A. K., 1982: Saturation Point Analysis of Moist Convective Overturning. *J. Atmos. Sci.*, **39**, 1484-1505.

Betts, A.K., 1992: FIFE Atmospheric Boundary Layer Budget Methods. *J. Geophys. Res.*, **97**, 18523-18532.

Betts, A.K., 2003: Diurnal Cycle. *Encyclopedia of Atmospheric Sciences*, J. R. Holton J. Pyle and J. A. Curry, Eds., Academic Press, London, pp. 640-643.

Betts, A. K., 2004: Understanding Hydrometeorology using global models. *Bull. Amer. Meteorol. Soc.*, **85**, 1673-1688.

Betts, A. K., 2006: Radiative scaling of the nocturnal boundary layer and the diurnal temperature range. *J. Geophys. Res.*, **111**, D07105, doi:10.1029/2005JD006560.

Betts, A. K., 2007: Coupling of water vapor convergence, clouds, precipitation, and land-surface processes. *J. Geophys. Res.,* **112**, D10108, doi:10.1029/2006JD008191.

Betts, A.K. and W. L. Ridgway, 1989: Climatic equilibrium of the atmospheric convective boundary layer over a tropical ocean. *J. Atmos. Sci.*, **46**, 2621-2641.

Betts, A.K. and J.H. Ball, 1994: Budget analysis of FIFE-1987 sonde data. *J. Geophys. Res.*, **99**, 3655-3666.

Betts, A.K. and J.H. Ball, 1995: The FIFE surface diurnal cycle climate. *J. Geophys. Res.* **100**, 25679-25693.

Betts, A. K. and J. H. Ball, 1997: Albedo over the boreal forest. *J. Geophys. Res.*, **102**, 28901-28910.

Betts, A. K. and J. H. Ball, 1998: FIFE surface climate and site-average dataset: 1987-1989. *J. Atmos. Sci.*, **55,** 1091-1108.

Betts, A. K and P. Viterbo, 2005: Land-surface, boundary layer and cloud-field coupling over the southwestern Amazon in ERA-40. *J. Geophys. Res.*, **110**, D14108, doi:10.1029/2004JD005702.

Betts, A. K., J.H. Ball, A.C.M. Beljaars, M.J. Miller and P. Viterbo, 1996: The land-surface-atmosphere interaction: a review based on observational and global modeling perspectives. *J. Geophys. Res.,* **101**, 7209-7225.

Betts, A. K., P. Viterbo, A.C.M. Beljaars and B.J.J.M. van den Hurk, 2001a: Impact of BOREAS on the ECMWF Forecast Model. *J. Geophys. Res.*, **106,** 33593-33604.

Betts, A. K., J. H. Ball, and J. H. McCaughey, 2001b: Near-surface climate in the boreal forest. *J. Geophys. Res.*, **106**, 33529-33542.

Betts, A.K., J. Ball, A. Barr, T. A. Black, J. H. McCaughey and P. Viterbo, 2006: Assessing land-surface-atmosphere coupling in the ERA-40 reanalysis with boreal forest data. *Agricultural and Forest Meteorology*, **140**, 355-382, doi:10.1016/j.agrformet.2006.08.009. Also available as http://www.ecmwf.int/publications/library/ecpublications/_pdf/era40/ERA40_PRS26_rev1.pdf

Betts, A. K., M. Köhler and Y-C. Zhang, 2008a: Comparison of river basin hydrometeorology in ERA-Interim and ERA-40 with observations. *J. Geophys. Res.* (submitted). Available as
http://www.ecmwf.int/publications/library/ecpublications/_pdf/tm/501-600/tm568.pdf

Betts, A.K., M.A.F. Silva Dias, G. Fisch, C. von Randow, J.C.P. Cohen, R. da Silva, D.R. Fitzjarrald, 2008b. The Amazonian Boundary layer and mesoscale circulations. Chapter B3 in IGBP Synthesis Vol. *Amazonia and Global Change*. Eds. M. Keller, J. Gash, P. Silva Dias. 2008BK000725R (in press).

Betts, R.A., 2000: Offset of the potential carbon sink from boreal forestation by decreases in surface albedo. *Nature,* **408**, 187–190.

Dirmeyer, P. A., R. D. Koster, and Z. Guo, 2006: Do global models properly represent the feedback between land and atmosphere? *J. Hydrometeor. 7*, 1177-1198.

Fischer, E. M., S. I. Seneviratne, D. Lüthi and C. Schär, 2007: Contribution of land-atmosphere coupling to recent European summer heat waves. *Geophys. Res. Lett.*, **34**, L06707, doi:10.1029/2006GL029068.

Hall F.G., A.K. Betts, S. Frolking, R. Brown, J. M. Chen, W. Chen, S. Halldin, D. P. Lettenmaier, and J. Schafer, 2004: The boreal climate. Chapter 7 in *Vegetation, Water, Humans and the Climate: a New Perspective on an Interactive System,* A Synthesis of the IGBP Core Project, Biospheric Aspects of the Hydrological Cycle, Eds, Kabat et al., Springer, Berlin, Heidelberg, New York, pp. 93-114. ISSN 1619-2435, ISBN 3-540-42400-8.

Higgins, R. W., W. Shi, E. Yarosh, R. Joyce, 2000: Improved United States Precipitation Quality Control System and Analysis", NCEP/Climate Prediction Center ATLAS No. 7, U. S. Department of Commerce, National Oceanic and Atmospheric Administration, National Weather Service.

Koster, R.D. and 25 co-authors, 2006: GLACE: The Global Land Atmosphere Coupling Experiment. Part 1. Overview. *J. Hydrometeor.*, **7**, 590-610.

Maurer, E.P., A.W. Wood, J.C. Adam and D.P. Lettenmaier, 2002: A long-term hydrologically based dataset of land-surface fluxes and states for the conterminous United States. *J. Climate, 15*, 3237-3251.

McNaughton, K. G., 1976: Evaporation and Advection I: Evaporation from Extensive Homogeneous Surfaces, *Quart. J. Roy. Meteorol. Soc.* **102***, 181-191.

Priestley, C. H. B. and Taylor, R. J., 1972: On the Assessment of Surface Heat Flux and Evaporation, *Mon. Wea. Rev.* **106**, 81-92.

Sellers, P.J., F.G Hall, G. Asrar, D.E. Strebel and R. E Murphy, 1992: An overview of the First International Land Surface Climatology Project (ISLSCP) Field Project (FIFE). *J. Geophys. Res.*, **97**, 19345-18371.

Sellers, P. J. and 20 co-authors, 1997: BOREAS in 1997: Experiment overview, scientific results and future directions. *J. Geophys. Res.*, **112**, 28731-28769.

Seneviratne, S. I., D. Lüthi, M. Litschi and C. Schär, 2006: Land–atmosphere coupling and climate change in Europe. *Nature*, **443**, 14 September2006, doi:10.1038/nature05095.

Uppala, S.M. and 45 co-authors, 2005: The ERA-40 Reanalysis. *Quart. J. Roy. Meteorol. Soc,* **131**, 2961-3012.

Van den Hurk, B.J.J.M., P. Viterbo, A.C.M. Beljaars and A. K. Betts, 2000: Offline validation of the ERA-40 surface scheme. ECMWF Tech Memo, 295, 43 pp., Eur. Cent. For Medium-Range Weather Forecasts, Shinfield Park, Reading RG2 9AX, England, UK.
http://www.ecmwf.int/publications/library/ecpublications/_pdf/tm/001-300/tm295.pdf

Viterbo, P. and A.C.M. Beljaars, 1995: A new land surface parameterization scheme in the ECMWF model and its validation. *J. Clim.,* **8**, 2716-2748.

Viterbo, P. and A.K. Betts, 1999: The impact on ECMWF forecasts of changes to the albedo of the boreal forests in the presence of snow. *J. Geophys. Res.*, **104**, 27 803-27 810.

Von Randow, C., A. O. Manzi, B. Kruijt, P. J. de Oliveira, F. B. Zanchi, R. L. Silva, M. G. Hodnett, J. H. C. Gash, J. A. Elbers, M. J. Waterloo, F. L. Cardoso, and P. Kabat, 2004: Comparative measurements and seasonal variations in energy and carbon exchange over forest and pasture in south west Amazonia, *Theor. and Appl. Climatol.*, **78**, 5-26.

Zhang, Y.-C., W. B. Rossow and P. W. Stackhouse, Jr., 2007: Comparison of different global information sources used in surface radiative flux calculation: Radiative properties of the surface. *J. Geophys. Res.,* **111***, D01102, doi:10.1029/2005JD007008.